J. Fluid Mech. (1986), *vol.* 169, *pp.* 211–227
Printed in Great Britain

Three-dimensional buoyancy-driven flows in cylindrical cavities with differentially heated endwalls. Part 1. Horizontal cylinders

By P. BONTOUX, C. SMUTEK, B. ROUX
Institut de Mécanique des Fluides, Université d'Aix – Marseille II, Marseille, France

AND J. M. LACROIX
I.M.S.P., Université de Nice, Nice, France

(Received 27 September 1984 and in revised form 6 February 1986)

Numerical solutions of the three-dimensional equations for buoyancy-driven flows in cylinders with differentially heated endwalls have been obtained by a finite-difference method. Special attention has been devoted to the complex three-dimensional flow structures arising in horizontal cylinders for configurations relevant for crystal growth by vapour transport. The characterization of the transition between the core-driven regime and the boundary-layer-driven regime is considered with the properties of the main flow and also the transverse flow.

1. Introduction

The buoyancy-driven flows (natural convection) in cylinders with differentially heated endwalls (axial temperature gradient) is a topic of practical interest for many applications, particularly for materials processing. Crystallization from vapours (physical and chemical vapour transport) has gained ever increasing importance in the preparation of semi-conductors, insulators and metals. Rosenberger (1980) detailed the advantages of vapour growth over crystallization from melts as resulting mainly from the lower temperatures involved. For most of such applications the growth ampoules are circular cylinders with large aspect ratios (length/radius) which are placed in horizontal furnaces producing an axial temperature gradient. But some crystal-growth experiments are also done in a microgravity environment, and in this case the furnace axis can present an angle with the residual gravity vector.

Horizontal cylinders, but with heating from the sidewalls, have been studied experimentally by Martini & Churchill (1960) and numerically by Leong & de Vahl Davis (1979) and Leong (1983). For the cylinders with differentially heated endwalls considered here, asymptotical theories have been proposed for large aspect ratios and small Rayleigh numbers (Klosse & Ullersma 1973; Gershuni & Zhukhovitskii 1976; Bejan & Tien 1978) which enabled the axial velocity component to be found, with an S-shaped profile in the vertical symmetry plane, as in differentially heated rectangular cavities (Bontoux *et al.* 1986). In that case, the main motion corresponds to two horizontal counterflows moving from the hot wall above, and from the cold wall below. Computations were made by Hong (1977) and Kimura & Bejan (1980*a*) to determine the motion in the median ($\bar{z} = \frac{1}{2}L$) cross-section as a solution of

two-dimensional (r, ϕ)-equations. These last authors numerically confirmed the existence of the four secondary eddies situated in the four quadrants of the median cross-section and superimposed onto the main counterflows, as revealed by the asymptotical theory developed to second order in $Ra\,k_1$ by Bejan & Tien (1978). Experiments were carried out at large Ra (Kimura & Bejan 1980*b*). Recent velocity measurements from Schiroky & Rosenberger (1984) detailed the structure of the flow in the whole $A = 10$ cylinder over a wide range of Ra and exhibited fully three-dimensional patterns in the end region. In this study too, an extension to third order of the series expansion in $Ra\,k_1$ given by Bejan & Tien (1978) was proposed. The validity limit of these asymptotical theories has been discussed in a previous paper by Bontoux *et al.* (1986).

The present paper has three purposes. The first is related to the validity of the numerical approximation with respect to accurate and detailed experimental results (Schiroky 1982; Schiroky & Rosenberger 1984). The second is to give a detailed description of the three-dimensional flow field in the horizontal cylinder, some features in the symmetry plane and the end regions being shown in the experiments. The third is an extension of the analysis of the flow regimes (core-driven regime, boundary-layer-driven regime) discussed by Bontoux *et al.* (1986). Here the characterization of the regimes' transition involves the properties of the transverse flow. The results concern vapour transport ($Pr \sim 0.7$) in a long cylinder ($A = 10$) and are given for several values of Ra relevant for vapour-growth experiments.

The present numerical code is directly derived from the code CYL3D elaborated by Leong & de Vahl Davis (1979) and based on the ADI method (Mallinson & de Vahl Davis 1973) with the vorticity-velocity formulation. But is has been carefully adapted for efficient use on a vector computer, not only to save computation time, but mainly to allow for the computation of the most severe flow configurations corresponding to the boundary-layer regime in long cylinders.

2. Physical and mathematical models

The cylindrical enclosure is defined by the radius R, the length L, and the inclination γ with respect to the gravity vector $\boldsymbol{g}$. The aspect ratio is defined by $A = L/R$. At a point $(\bar{r}, \phi, \bar{z})$ in the cylindrical reference frame, the velocity $\boldsymbol{U}$ has the components $(\bar{u}, \bar{v}, \bar{w})$. The cavity is differentially heated by the two isothermal endwalls (at $\bar{z} = 0$ and $\bar{z} = L$) with a total temperature difference of $\Delta T = T_h - T_c$. The sidewalls ($\bar{r} = R$) are perfectly conducting.

The mathematical model is given by the Navier–Stokes and energy equations with the simplified Boussinesq approximation (Joseph 1976). Using R and χ/R as scaling factors for the length and the velocity respectively and cylindrical coordinates (see the figure 1), the system is described by the vorticity $\boldsymbol{\zeta}(\zeta_r, \zeta_\phi, \zeta_z)$, the temperature $\theta = 2(T - T_0)/\Delta T$ and the velocity $\boldsymbol{U}$ as dependent variables, (Leong & de Vahl Davis 1979; Leong 1983):

$$\boldsymbol{\nabla} \times (\boldsymbol{U} \times \boldsymbol{\zeta}) = \tfrac{1}{2} Ra\, Pr(\boldsymbol{\nabla} \times \theta \hat{\boldsymbol{g}}) + Pr\, \boldsymbol{\nabla} \times (\boldsymbol{\nabla} \times \boldsymbol{\zeta}), \tag{1}$$

$$\boldsymbol{\nabla}^2 \boldsymbol{U} = -\boldsymbol{\nabla} \times \boldsymbol{\zeta}, \tag{2}$$

$$\boldsymbol{\nabla} \cdot (\boldsymbol{U}\theta) = \boldsymbol{\nabla}^2 \theta, \tag{3}$$

where the Rayleigh number Ra is defined by the Grashof number, $Gr = \beta g \Delta T R^3/\nu^2$ and the Prandtl number $Pr = \nu/\chi$ as $Ra = Gr\, Pr$. $\hat{\boldsymbol{g}}$ is the unity gravity vector and $T_0 = \frac{1}{2}(T_h + T_c)$.

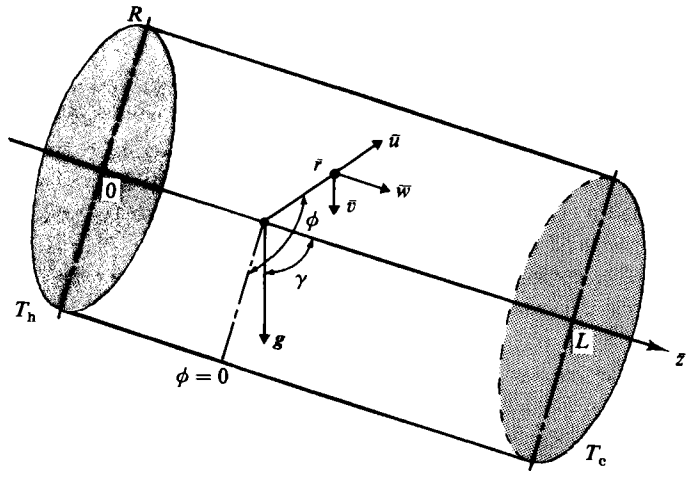

FIGURE 1. Geometry of the enclosure and frame of reference, with hot (T_h) and cold (T_c) circular walls.

Specific scalings could be used when buoyancy terms balance either inertia terms (large Gr or small Pr) or viscous terms (small Gr or large Pr). In the present analysis, which considers moderate values of Gr and Pr, the 'standard' scaling used by de Vahl Davis and co-workers (Mallinson & de Vahl Davis 1973, 1977; Mallinson, Graham & de Vahl Davis 1981), appeared to be a good compromise.

The aspect ratio A, which appears in the boundary conditions, is not explicit in the system (1)–(3), because a common lengthscale R is used for r- and z-variables. The choice of Ra based on lengthscale R is particularly suitable for long cylinders, as shown by asymptotical laws (see §4).

The vorticity-velocity formulation proposed by Fasel (1979) involves simpler boundary conditions for the three Poisson equations (2) on the three velocity components, compared to the vorticity-vector potential formulation. (It also requires less arrays.) For rigid walls the usual no slip conditions apply: $u = v = w = 0$.

The boundary conditions for the vorticity on rigid walls are derived from these velocity conditions:

at the endwalls ($z = 0, A$)

$$\zeta_r = -\frac{\partial v}{\partial z}, \quad \zeta_\phi = \frac{\partial u}{\partial z}, \quad \zeta_z = 0; \tag{4}$$

at the sidewalls ($r = 1$)

$$\zeta_r = 0, \quad \zeta_\phi = -\frac{\partial w}{\partial r}, \quad \zeta_z = \frac{\partial v}{\partial r}. \tag{5}$$

The thermal boundary conditions correspond to isothermal endwalls, $\theta = \pm 1$, and a linear temperature profile on the sidewalls, $\theta = 1 - 2z/A$.

3. Solution method

The method used has been elaborated by Leong & de Vahl Davis (1979). It consists of a centred finite-difference scheme with a uniform mesh composed of $\hat{L} \times \hat{M} \times \hat{N}$ discretizing points in the (r, ϕ, z)-directions. As proposed by de Vahl Davis (1979), there is no mesh point along the axis in order to avoid the problem of singularity.

The step size is $\Delta r = (\hat{L}-0.5)^{-1}$ and the first mesh point is at $\frac{1}{2}\Delta r$ from the axis where second-order forward differences are used. The azimuth $\phi = 0$ is chosen to correspond to the half vertical plane below the axis (see figure 1).

The Poisson equations (2) with Dirichlet conditions are solved with a Fourier solver (Le Bail 1972) which uses the FFT algorithm developed by Cooley & Tukey (1965).

The ADI scheme of Samarskii–Andreyev is used with a false transient technique for the transport equations (1) and (3) (see Mallinson & de Vahl Davis 1973; Leong & de Vahl Davis 1979; Leong 1983). This scheme gives rise to tridiagonal algebraic systems which are solved by the Thomas algorithm.

For steady-state solutions, the convergence is accelerated by using relaxation factors, respectively α_ζ and α_θ, in the (false) transient terms of the transport equations.

The code is run on a vector computer (CRAY 1/S1000). The efficiency of the method has been improved in terms of computing time by 'vectorizing' the highly serial algorithms (FFT and Thomas). Details are given in previous papers by Smutek *et al.* (1983, 1985).

The mesh sizes used were from $11 \times 16 \times 17$ up to $9 \times 32 \times 129$ for the horizontal cylinder with $A = 10$. The accuracy of the solutions was checked by evaluating the divergence of $\boldsymbol{U}$ which is not set identically to zero with the vorticity-velocity formulation.

4. Convection regimes

The basic motion in long differentially heated cylinders corresponds to two horizontal counterflows moving from the hot wall, above, and from the cold wall, below (see Bejan & Tien 1978). A similar basic flow also exists in horizontal shallow rectangular boxes, studied by Cormack, Leal & Imberger (1974*a*), Cormack, Leal & Seinfeld (1974*b*) and Imberger (1974), which exhibit the following main features:

At small Ra, the horizontal temperature gradient is constant in the core and the main buoyancy forces are located there (core-driven regime). The role of the vertical endwalls is only to turn the flow, which is parallel to the axis everywhere else.

At larger Ra, the main buoyancy forces are located in the end regions where both thermal and dynamical boundary layers develop (boundary-layer-driven regime), while the core plays only a passive role.

In cylinders, this basic flow was studied with an asymptotic theory by Bejan & Tien (1978) who develop dimensionless velocity variables in a power-series expansion of $Ra\,k_1$ as follows:

$$(u, v, w) = (u, v, w)_{\mathrm{I}}\, Ra\, k_1 + (u, v, w)_{\mathrm{II}}\, (Ra\, k_1)^2 + (u, v, w)_{\mathrm{III}}\, (Ra\, k_1)^3 + \ldots, \qquad (6)$$

where k_1 is the horizontal temperature gradient in the core defined as $k_1 = -0.5\,\partial\theta/\partial z$. At low Ra, (core-driven regime), $k_1 = R/L$ and the first-order terms yield S-shaped profiles for the axial velocity which have been shown to predict accurately the flow in the middle part ($z \approx \frac{1}{2}A$) of the symmetry plane of the cylinder (Bontoux *et al.* 1986):

$$\left.\begin{aligned} u_{\mathrm{I}} &= v_{\mathrm{I}} = 0, \\ w_{\mathrm{I}} &= \tfrac{1}{8}(r^2-1)\, r \cos\phi. \end{aligned}\right\} \qquad (7)$$

Weak three-dimensional flow structures are superimposed onto the main counterflows in the core as revealed by the second-order terms of the expansion (Bejan & Tien 1978;

and Shih 1981) and confirmed by the two-dimensional computations in the median ($z = \frac{1}{2}A$) cross-section (Kimura & Bejan 1980*a*):

$$\left.\begin{aligned} u_{\mathrm{II}} &= -\frac{(2r^6-15r^4+24r^2-11)\,r}{184\,320}\cos 2\phi, \\ v_{\mathrm{II}} &= \frac{(-8r^6+45r^4-48r^2+11)\,r}{184\,320}\sin 2\phi, \\ w_{\mathrm{II}} &= 0. \end{aligned}\right\} \tag{8}$$

The third-order terms of such an expansion would give a representation of the shift of the maximal velocity toward the wall (Schiroky & Rosenberger 1984). But this improvement is limited to a small range of Ra very close to the beginning of the boundary-layer-driven regime.

For an $A = 10$ cylinder, experiments by Schiroky & Rosenberger (1984) based on laser-Doppler anemometry exhibited strong three-dimensional flow structures in the vicinity of the hot and cold walls for $Ra \geqslant 3580$. In these experiments, boundary layers are shown to develop simultaneously along the end- and sidewalls.

4.1. *Convergence and accuracy*

The convergence is accelerated by taking an initial condition obtained from the first-order solution (7) and the matching function

$$e(z) = \tanh\left[48(A-z)^2\frac{z^2}{A^4}\right]. \tag{9}$$

The convergence of the solution toward a steady state is shown in figure 2 for different Ra values at $A = 10$ with a $9\times32\times33$ mesh. This figure shows the axial velocity w at the point $(4,4,4)$ close to the hot wall. For $Ra = 660$, convergence is obtained after only 30 iterations. At $Ra = 3580$, it is reached after 60 iterations from the $Ra = 660$ solution. For this Ra, a direct computation from (7) and (9) as initial conditions converges in the same number of iterations. However after the transition to the boundary-layer regime ($Ra = 18720$), an adapted value of k_1 ($k_1 < 0.10$) is necessary for convergence when (7) and (9) are used. On figure 2 the initial condition for this case corresponds to the $Ra = 8860$ converged solution. The time-step size is defined by $\Delta t = 0.5$ min $(\Delta r^2, \Delta\phi^2, \Delta z^2)$ and is used with optimal values for the false transient factors, which vary strongly with Ra. They have been selected such that $\alpha_\theta \approx 10\,\alpha_\xi$, with α_θ ranging from 20 to 1 when Ra is increased from 660 to 18720.

With the vorticity-velocity formulation the discrete continuity equation is not implicitly satisfied by the computed solution, as with the vorticity-vector potential formulation. The difference to zero of the discretized divergence of $\boldsymbol{U}$ can be used to control the accuracy of the solution. The values of 4 div $\boldsymbol{U}/(\sqrt{3}\,Ra)$ calculated for different z at $r \approx 0.53$ in the plane $\phi = 0$ are plotted in figure 3 for $Ra = 3580$. They are close to zero for most of the values of z except near the two endwalls where they present two maxima. Figure 3 also shows that these maxima diminish rapidly when the mesh size is reduced.

In the core the accuracy is also controlled through the mesh dependency of some characteristic solutions. Comparisons are also made with available experiments. Fig. 4 represents the axial velocity profiles in the vertical symmetry plane with $11\times16\times17$ and $9\times32\times33$ mesh points. These two kinds of solution are very close and agree with the experimental values given by Schiroky & Rosenberger (1984) at

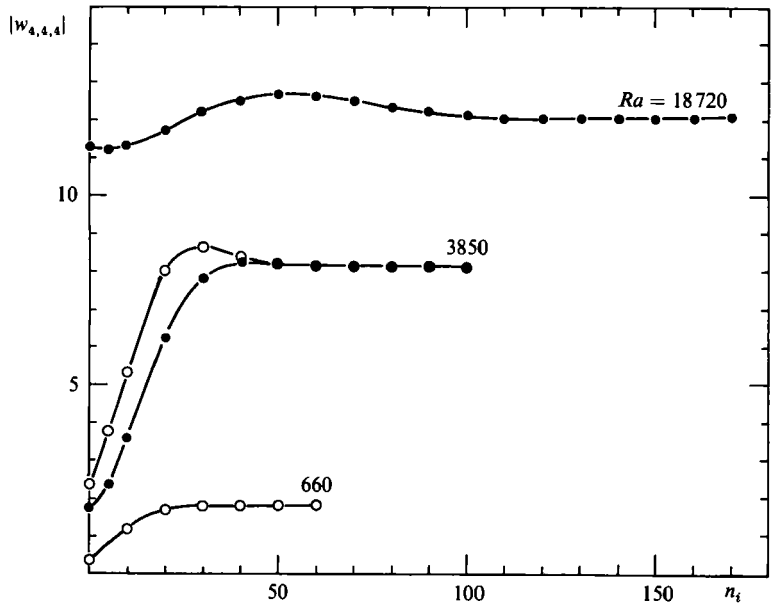

FIGURE 2. Convergence of w-solution versus iterations number n_i in a horizontal cylinder ($\gamma = 90°$); $A = 10$, $Pr = 0.73$. Starting conditions: ○, relations (7) and (9); ●, converged solution at lower Ra.

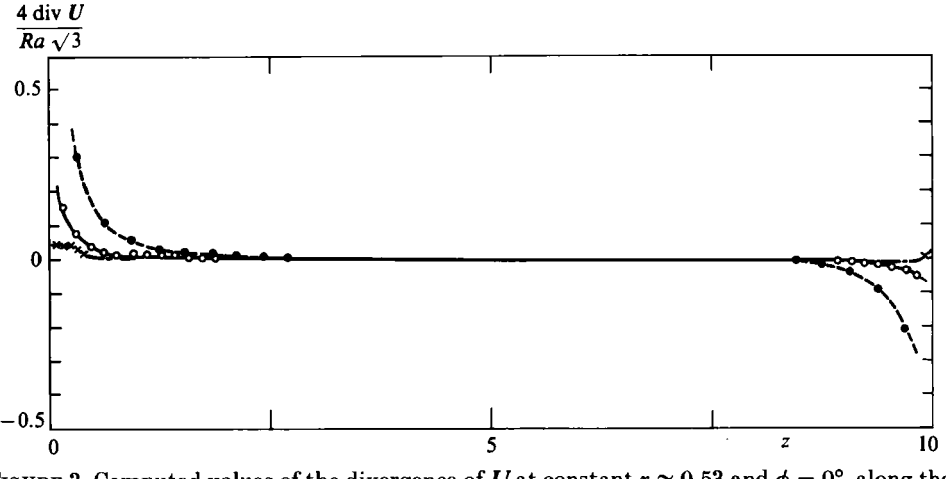

FIGURE 3. Computed values of the divergence of U at constant $r \approx 0.53$ and $\phi = 0°$, along the axis. Effect of the mesh size at $Ra = 3580$, $Pr = 0.73$ and $A = 10$. Mesh: ●, $9 \times 32 \times 33$; ○, $9 \times 32 \times 65$; ×, $9 \times 32 \times 129$.

$Ra = 660$, 3580 and 18720. Additional computations carried out with more than 33 points along the axis have shown that the numerical solution is not very substantially modified in the core.

A larger influence of the mesh size is observed near the endwalls, where the boundary layers develop (figures 5*a*, *b*). To be well represented the u-solution needs 65 points along the axis when $3850 \leqslant Ra \leqslant 18720$. The $9 \times 32 \times 129$ solution makes no significant differences to the values of u. It is to be noted that the computation

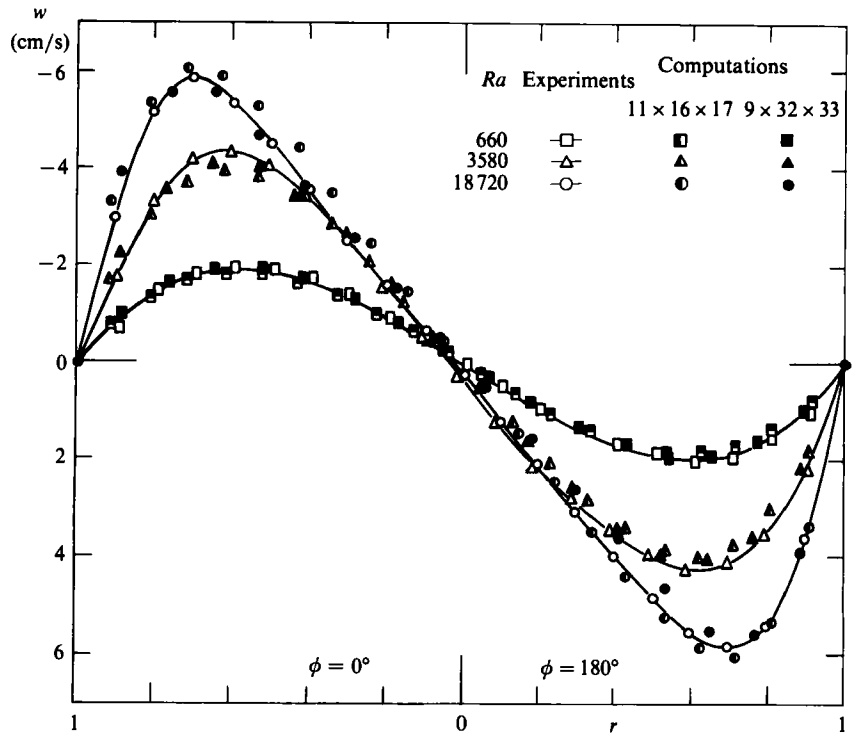

FIGURE 4. Axial velocity profiles versus radius. Effect of the mesh size and comparisons with the experiments of Schiroky & Rosenberger (1984); $A = 10$, $Pr = 0.73$.

underpredicts the experimental data (which are given only for the cold endwalls) by about 17–20%. Although the influence of smaller radial step sizes was not explicitly checked in that case, we think that this difference between numerical and experimental results is more probably connected to an effect of variation of density and viscosity (neglected in the present model), and to a possible defect of insulation at the endwalls (in the experiments) as suggested by Leonardi (1984).

4.2. *Regimes and transition (symmetry-plane solution)*

The core-driven regime is characterized by flow parallelism in the core and independence in the z-direction. The values of the axial velocity are plotted in figure 6 for $A = 10$ along lines parallel to the axis at $r \approx 0.53$ and $\phi = 180°$ for $Ra \leqslant 18720$. The independence from z is verified over more than 50% of the length up to $Ra = 1830$. It decreases to about 30% at $Ra = 3580$. Above $Ra = 6000$, the dependency on z becomes important. This also gives a limit to Ra beyond which the asymptotic theory cannot be used.

The values of the maximum for the axial and crossflow velocities in the core may be derived from relations (7) and (8) as follows:

$$w_{\max}^{\text{th}} = \frac{Ra\, k_1}{12\sqrt{3}}, \tag{10}$$

$$(u, v)_{\max}^{\text{th}} \approx 1.65 \times 10^{-5} (Ra\, k_1)^2. \tag{11}$$

They are shown for $A = 10$ ($k_1 = 0.1$) on figure 7 together with the present results and with the experimental data (limited to w) given by Schiroky & Rosenberger

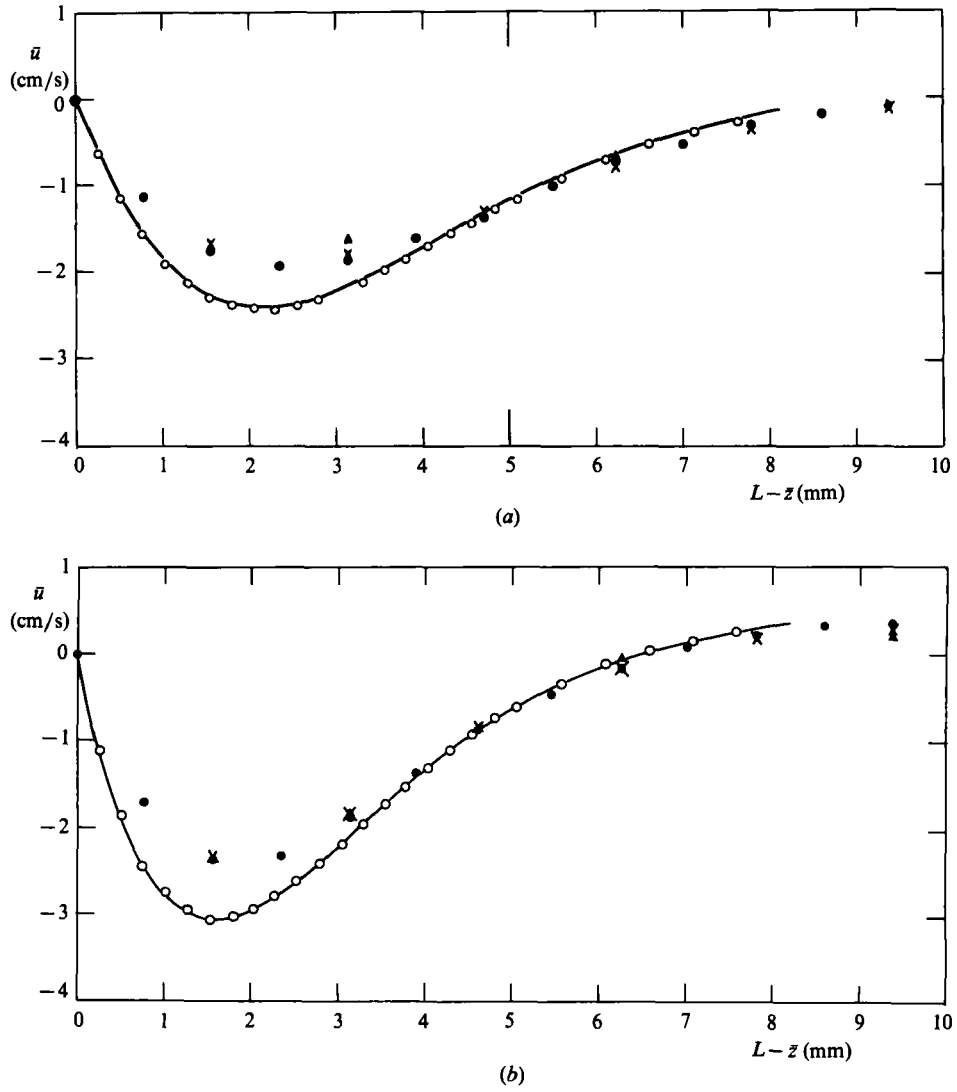

FIGURE 5. Vertical velocity profiles along the axis. Effect of the mesh size at $A = 10$, $Pr = 0.73$ with (*a*) $Ra = 3580$; (*b*) 8860. Mesh: ▲, $9 \times 32 \times 33$; ×, $9 \times 32 \times 65$; ●, $9 \times 32 \times 129$; –○–, comparisons with the experiments of Schiroky & Rosenberger (1984).

(1984). The numerical and experimental values of $w_{\max}$ in the median cross-section move away from (10) with a $Ra^{\frac{1}{2}}$ trend when $Ra \gtrsim 6000$, but they are in perfect agreement with the analytical solution for lower Ra. The numerical values of $u_{\max}$ are in good agreement with the theory for small Ra and move more gradually away from (11) after $Ra \approx 1000$. After a certain value $Ra \approx 3000$, for which $u_{\max}$ is about one tenth of $w_{\max}$, they seem to vary as $Ra^{0.85}$.

An extreme upper limit for the parallel flow (and the core-driven regime) could be deduced from (10) and (11) as the intersection of the two theoretical curves, which could correspond to $w = u$:

$$Ra_c k_1 \approx 2916,$$

that is

$$Ra_c \approx 29160 \quad \text{for} \quad A = 10.$$

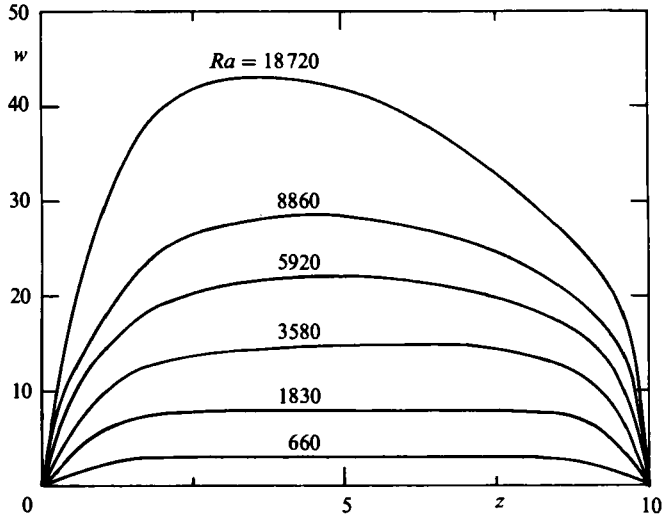

FIGURE 6. Variation of w at constant r, along the axis at $A = 10$, $Pr = 0.73$ and for various Ra.

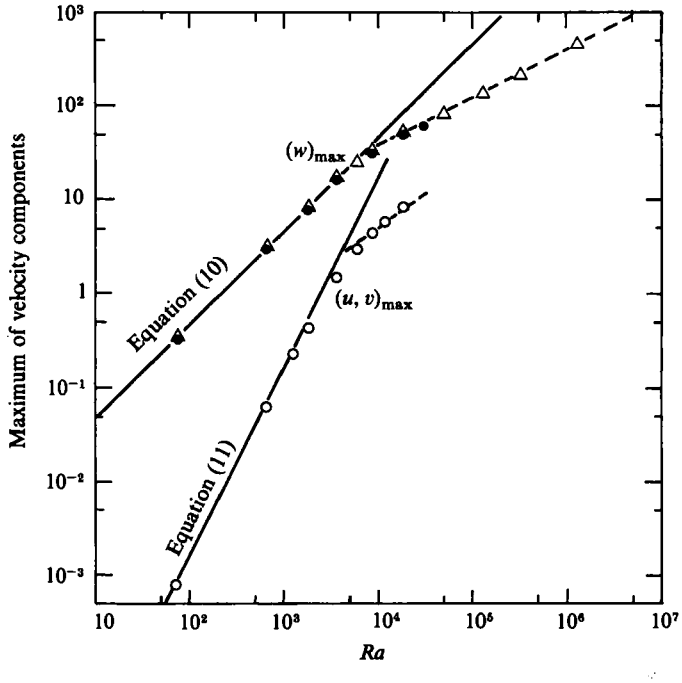

FIGURE 7. Variation of the maxima of w and (u, v) with Ra at $A = 10$, $Pr = 0.73$. Comparisons between experiments (△, w) (Schiroky & Rosenberger 1984), computations (○, (u, v)); (●, w), and theory (equations (11) for (u, v) and (10) for w) (Bejan & Tien 1978).

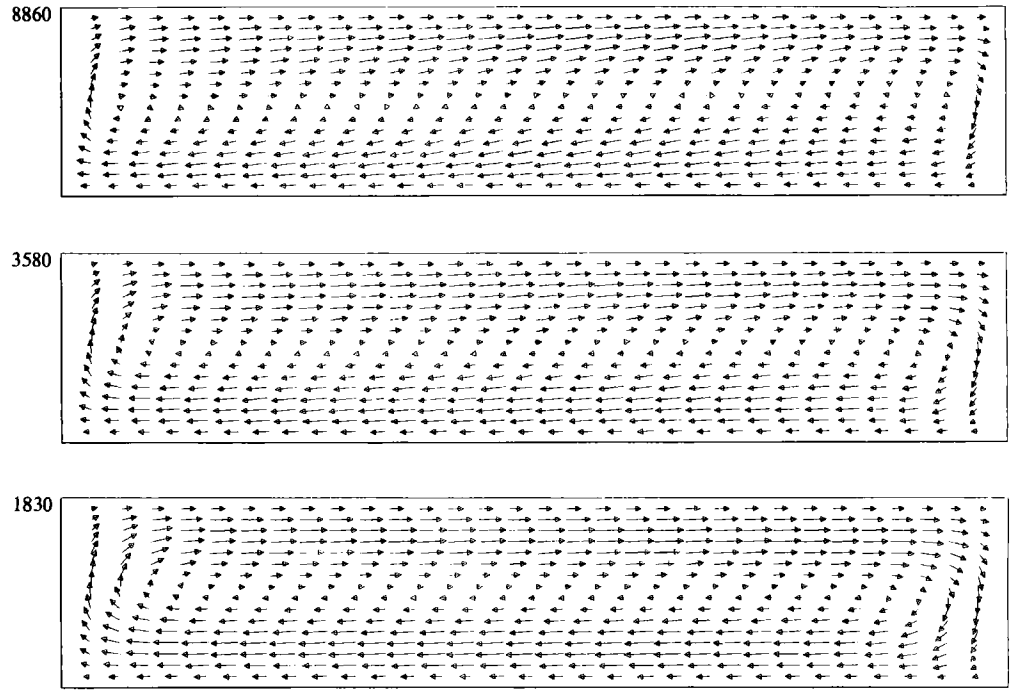

FIGURE 8. Velocity field in the vertical symmetry plane at $Ra = 8860$, 3580, and 1830, with $A = 10$, $Pr = 0.73$.

A more realistic value of Ra_c, as the limit of quasi-parallel flow, could be characterized by $u^{th}_{max}/w^{th}_{max} = 10\,\%$. Then

$$Ra_c \approx 2916 \quad \text{for} \quad A = 10. \tag{12}$$

Other critical Rayleigh numbers could be based on a 10 % deviation of w_{max} from (10), as in a previous paper by Bontoux *et al.* (1986), or of u_{max} from (11). They could give, respectively,

$$Ra_c \approx 5920 \quad \text{for} \quad |w_{max} - w^{th}_{max}| \approx 0.1\, w^{th}_{max}, \tag{13}$$

$$Ra_c \approx 1830 \quad \text{for} \quad |u_{max} - u^{th}_{max}| \approx 0.1\, u^{th}_{max} \tag{14}$$

The u-component appears to deviate sooner from asymptotical law and the criterion (12) seems to give a good compromise in characterizing the end of the conducting regime for long cylinders as the limit of quasi-parallel flow.

The characteristic flow patterns in the vertical symmetry plane are shown in figures 8 and 9 for Ra ranging from 1830 to 18720 (including the regime of transition). These figures exhibit the main features of the flow in this plane: flow parallelism up to $Ra = 1830$ and flow inclination above, with the onset of secondary vortices in the end regions at $Ra = 8860$. These secondary vortices have been previously observed in experiments (Ostrach, Loka & Kumar 1980) and by numerical simulations in two-dimensional cavities (Wirtz & Tseng 1980).

4.3. *Three-dimensional flow structure*

4.3.1. The projection of the velocity in the (r, z)-planes is shown at $Ra = 18720$ in figure 9 where ϕ is varied from 0° to 90°. The main feature in the core is the inclination of the flow with respect to the axis when $\phi = 0°$. At $\phi = 45°$, the flow is roughly

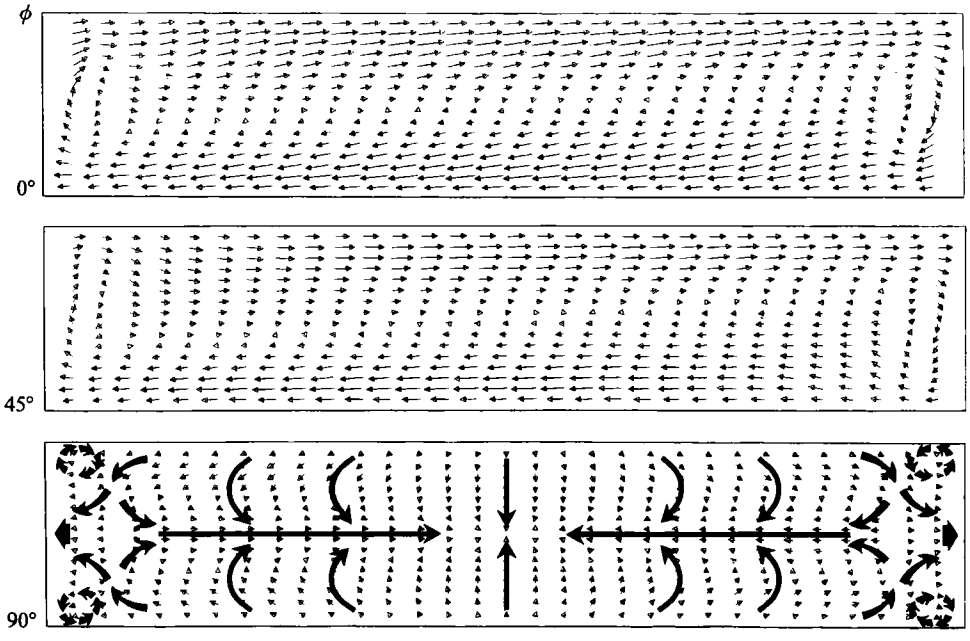

FIGURE 9. Velocity field in the $\phi = 0°$, 45° and 90° planes at $Ra = 18720$, $Pr = 0.73$ and $A = 10$.

parallel. Above this value of ϕ, the flow is organized into a general motion, shown for $\phi = 90°$ developing from the sides toward the middle point of the domain and into secondary motions located in the vicinity of the endwalls and directed toward them, with two rolls on each side.

4.3.2. In the horizontal mid-plane, the vertical motion was analysed by Schiroky & Rosenberger (1984) from measurements of the vertical velocity which show boundary layers development on the end- and sidewalls. The present code has been shown by Smutek *et al.* (1985) to predict qualitatively this three-dimensional pattern, even with a coarse mesh, such as $9 \times 32 \times 33$. The radial variation of the vertical velocity v given here with a finer mesh ($9 \times 32 \times 65$ and 129), at z corresponding to the maximum of v is shown in figure 10 for increasing Ra. When $Ra < 660$, the largest v is located in the symmetry plane. Above $Ra = 660$, two maxima of v are exhibited on each side of the symmetry plane, as in the experiments mentioned before. These maxima approach the sidewall when Ra is increased. At $Ra = 18720$ a zone of constant vertical velocity develops in the centre. The value of v in this internal region is less than about 20% of the maxima of v which are located at $r \approx 0.75$.

4.3.3. The cross-flow structure superimposed onto the main counterflows in the entire cavity is demonstrated in figure 11 at various vertical cross-sections (r, ϕ) between the hot wall and the centre. At the different Ra, four secondary eddies are found in the four quadrants of the median plane ($z = \frac{1}{2}A$), as predicted by the asymptotic theory (8) given by Bejan & Tien (1978). But these eddies expand differently along z when the endwalls are approached. Some differences occur at higher Ra due to the onset of the vortices in the vertical symmetry plane as mentioned before. The scales of axial and crossflow velocities defined in figure 7 indicate that a particle would turn

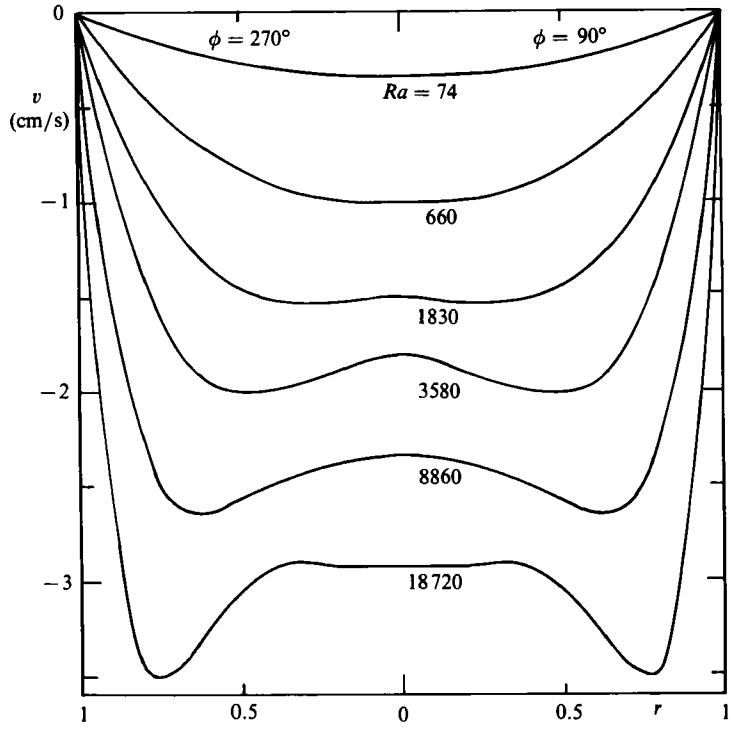

FIGURE 10. Vertical velocity profile v versus radius in the horizontal plane at z corresponding to the maximum of v; $A = 10$, $Pr = 0.73$.

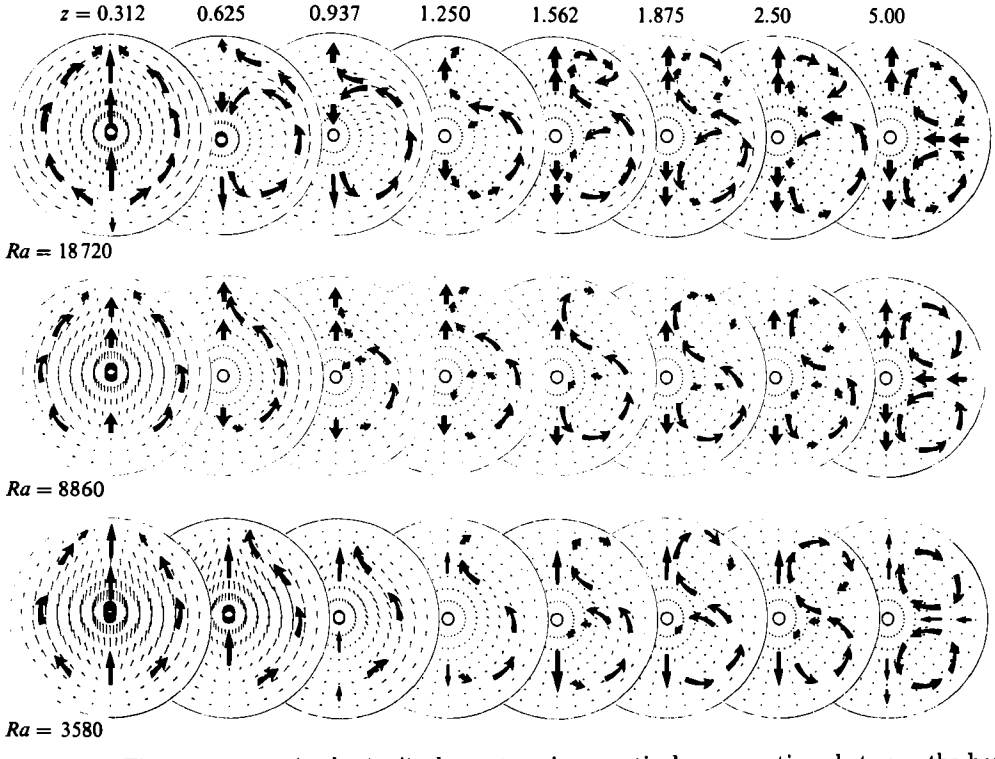

FIGURE 11. Flow structures in the (r, ϕ)-plane at various vertical cross-sections between the hot wall ($z = 0$) and the centre ($z = 5$) for $A = 10$; $Pr = 0.73$.

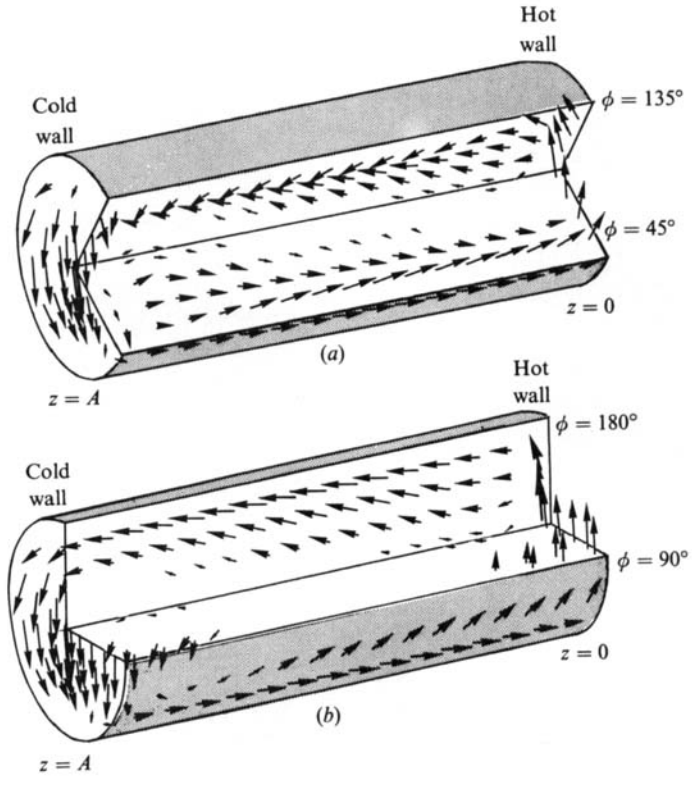

FIGURE 12. Three-dimensional velocity field (magnitude larger than 20% of the maximum) at various azimuths: (*a*) $\phi = 45°$ and 135° and (*b*) $\phi = 90°$ and 180°; $Ra = 18720$, $A = 10$.

through about 90° on the conical sheet between the hot and the cold walls at $Ra = 18720$.

4.3.4. In order to improve the flow depiction given by the plane projection of the velocity in the previous figures, the fully three-dimensional velocity pattern at $Ra = 18720$ is given in figure 12, at four regularly spaced azimuths: $\phi = 45°$ and $\phi = 135°$ (figure 12*a*) and $\phi = 90°$ and $\phi = 180°$ (figure 12*b*). The velocity vectors are plotted only when they exceed 20% of their maximum. In the regions hidden by the lateral (shaded) surfaces, they are only plotted at the last row ($i = 8$) in the r-direction, for given azimuths. The circular section at the far left of the cylinder on figure 12, corresponds to the first internal cross-section plane ($k = 64$) at a distance $z = 0.156$ from the cold endwall.

The analysis of the velocity pattern confirms the occurrence of low velocities (less than 20% of the maximum) everywhere in the horizontal mid-plane, except close to the endwalls. A secondary vortex sets in on the plane $\phi = 180°$ near the cold wall, inside the region without arrows (figure 12*b*). A symmetric one exists at $\phi = 0°$ near the hot wall. The influence zone of this last vortex is shown in figure 12*a* at $\phi = 45°$. This suggests the schematic representation of these vortices as 'crescent-shaped' regions, shown in figure 13.

Figure 12 (*a*) also reveals a strong deflection of the flow away from the symmetry plane in a '*peripheric*' layer flowing near the cylindrical wall. In the internal region the flow is generally inclined with respect to the axis as in the symmetry plane

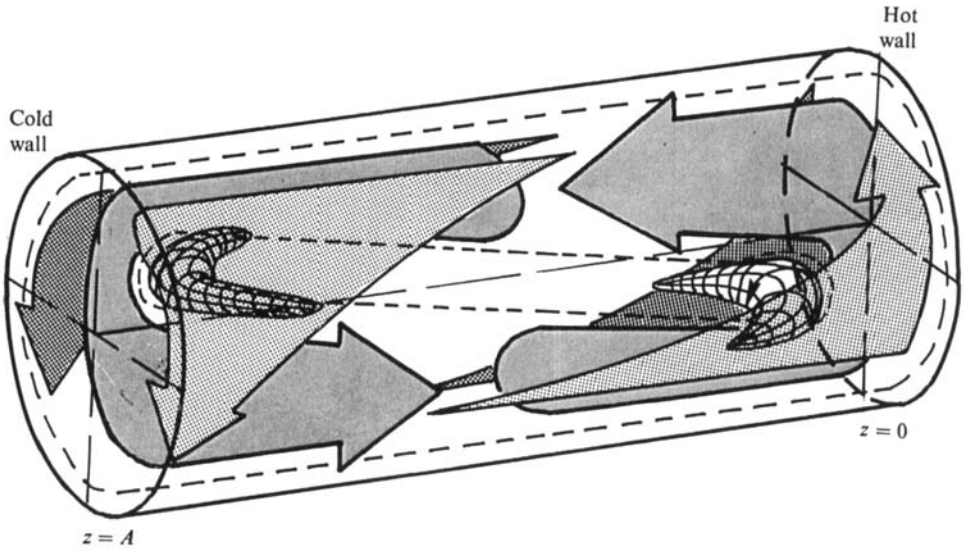

FIGURE 13. Schematic flow pattern in a horizontal cylinder at $A = 10$ and $Ra = 18720$. Primary and secondary flows.

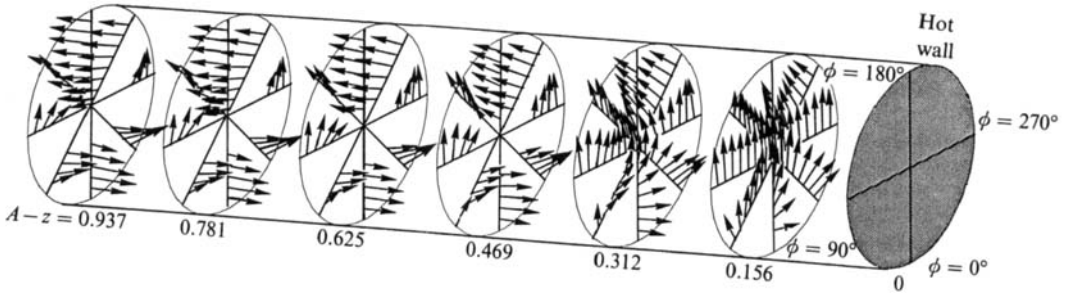

FIGURE 14. Three-dimensional velocity field (magnitude larger than 20% of the maximum) over a distance of $\frac{1}{10}A$ from the hot wall; $Ra = 18720$, $A = 10$.

($\phi = 180°$). In the peripheric layer the motion is driven from the flow generated along the vertical endwalls. In the upper part of the cylinder (above the horizontal mid-plane) the fluid begins to flow downward quite a way before reaching the cold end. Symmetrically, it is driven upward in the lower part of the cylinder.

The complete flow pattern, which admits symmetries with respect to the centre and to $\phi = 0°$, is schematically represented in figure 13 at $Ra = 18720$. The main flow seems to circulate in a 'tube' in the symmetry plane which is inclined with respect to the axis in the core of the cylinder. The deflection of the motion (crossflow effect) at the periphery of the 'tube' is also schematically represented by four arrows in figure 13.

The U-turning of the flow close to the hot end is emphasized in figure 14, over a distance of 10% of L, through velocity-vector fields plotted at several abscissae for regularly spaced azimuths.

In the lower part of the cylinder, the U-turning of the flow occurs at $\phi = 0°$ over a distance $0.3 \lesssim z \lesssim 0.5$, close to the hot endwall. Outside the symmetry plane, it arises much further away from this endwall (at $\phi = 90°$ and $\phi = 270°$ the magnitude of the vertical-velocity component reaches about 50% of the maximum). This confirms the limit of relevance of the two-dimensional models (symmetry-plane approximation) for high values of Ra, as previously discussed by Bontoux *et al.* (1986).

In the upper part of the cylinder, the reverse flow is concentrated in the sector $135° \lesssim \phi \lesssim 225°$, where it develops over the entire radii (including $r = 0$) for $z \lesssim 0.78$. The comparison of the arrows at $\phi = 135°$ and $225°$ suggests a tendency of the flow to converge towards the symmetry plane.

5. Conclusion

The fully three-dimensional buoyancy-driven gaseous flow ($Pr = 0.73$) in circular cylinders with differentially heated endwalls has been analysed with a finite-difference method which is basically a 'vectorized' version of the CYL3D code of Leong & de Vahl Davis (1979). Special attention has been devoted to long horizontal cylinders ($A = L/R = 10$).

For temperature gradients or Rayleigh numbers relevant for crystal growing by vapour transport in closed ampoules and including transition from the core-driven regime (low Ra) to the boundary-layer regime (higher Ra), detailed velocity fields (u, w-components) have been given in the vertical symmetry plane. In the core-driven regime, the flow is parallel to the axis. For higher Ra, an inclination of the flow with respect to the axis, characterized by the ratio u/w, appears and increases with Ra. A criterion for the upper limit of the core-driven regime is proposed from relevant analytical core solutions for u- and w-components. The criterion based on $u^{\text{th}}_{\max}/w^{\text{th}}_{\max} = 10\,\%$ gives $Ra_c \approx 2900$ for $A = 10$.

The flow field has also been identified near the endwalls (the cold endwall corresponding to the growing interface). The vertical velocity exhibits two maxima outside the symmetry plane for $Ra > 1830$, as in the experiments carried out by Schiroky & Rosenberger (1984). For $Ra = 18720$ the plotting of the three-dimensional velocity-vector field shows that the flow makes a U-turn close to the endwall at $\phi = 0°$. This turning occurs much earlier outside the symmetry plane, which confirms that a two-dimensional model (based on a symmetry-plane approximation) would not be very pertinent for Ra close to, or higher than, 18720. After the U-turn the flow comes back and is mostly concentrated in the sector $135° \lesssim \phi \lesssim 225°$.

Finally, the global flow structure has been analysed. A detailed analysis of the velocity components in vertical transverse cross-sections (at constant z or k) for several positions along the axis at $Ra = 3580$, 8860 and 18720, shows an helicoïdal motion rolling slightly on four conical sheets. A more informative depiction of such a flow structure has been given at $Ra = 18720$, through the three-dimensional velocity-vector field. A main flow driven from the endwall circulates in a 'tube', of variable section, surrounding a dead flow region limited by two 'crescent-shaped' vortices in the end region. This main flow starts from the hot wall in the upper part of the cylinder, turns down close to the cold wall and goes back towards the hot wall in the lower part of the cylinder. The flow at the periphery of the tube spreads into layers (crossflow) symmetric with respect to $\phi = 180°$, when reaching the cold wall.

The authors are indebted to S. S. Leong and G. de Vahl Davis for their code CYL3D and to F. Rosenberger's group for fruitful discussions of flow structure analysis in horizontal cylinders. They particularly acknowledge R. Peyret, R. Sani and P. G. Extremet for their advice during this work. Concerning the graphics of 3-D flow, they also wish to thank one of the reviewers and R. Sani for constructive criticisms and helpful suggestions.

The computations were carried out on the CRAY-1 of the CCVR (Centre de Calcul Vectoriel pour la Recherche). Research support by the C.N.R.S. (Centre National de

la Recherche Scientifique, GRECO 64), the D.R.E.T. (Direction des Recherches et Etudes Techniques, G.6) and the C.N.E.S. (Centre National d'Etudes Spatiales, Division Matériaux).

REFERENCES

BEJAN, A. & TIEN, C. L. 1978 Fully developed natural counterflow in a long horizontal pipe with different end temperatures. *Intl J. Heat Mass Transfer* **21**, 701–708.

BONTOUX, P., ROUX, B., SCHIROKY, G. H., MARKHAM, B. L. & ROSENBERGER, F. 1986 Convection in the vertical midplane of a horizontal cylinder. Comparison of 2-D approximations with 3-D results. *Intl J. Heat Mass Transfer* **29**, 227–240.

COOLEY, J. W. & TUKEY, J. W. 1965 An algorithm for the machine calculation of complex Fourier series. *Math. Comp.* **19**, 297–301.

CORMACK, D. E., LEAL, L. G. & IMBERGER, J. 1974*a* Natural convection in a shallow cavity with differentially heated end walls. Part 1. Asymptotic theory. *J. Fluid Mech.* **65**, 209–229.

CORMACK, D. E., LEAL, L. G. & SEINFELD, J. H. 1974*b* Natural convection in a shallow cavity with differentially heated end walls. Part 2. Numerical solutions. *J. Fluid Mech.* **65**, 231–246.

FASEL, H. F. 1979 Numerical solution of the complete Navier–Stokes equations for the simulation of unsteady flows. In *Approx. Methods for Navier–Stokes Problems IUTAM*. Lecture Notes in Mathematics, vol. 771, pp. 177–195. Springer.

GERSHUNI, G. Z. & ZHUKHOVITSKII, E. M. 1976 *Convective Stability of Incompressible Fluids*. Keters/Wiley.

HONG, S. W. 1977 Natural convection in horizontal pipes. *Intl J. Heat Mass Transfer* **20**, 685–691.

IMBERGER, J. 1974 Natural convection in shallow cavity with differentially heated end walls. Part 3. Experimental Results. *J. Fluid Mech.* **65**, 247–260.

JOSEPH, D. D. 1976 Stability of fluid motion II. *Tracts in Natural Philosophy*, vol. 28. Springer.

KIMURA, S. & BEJAN, A. 1980*a* Numerical study of natural circulation in a horizontal duct with different end temperatures. *Wärme- und Stoffürbertragung* **14**, 269–280.

KIMURA, S. & BEJAN, A. 1980*b* Experimental study of natural convection in a horizontal cylinder with different end temperatures. *Intl J. Heat Mass Transfer* **23**, 1117–1126.

KLOSSE, K. & ULLERSMA, P. 1973 Convection in a chemical vapor transport process. *J. Cryst. Growth* **18**, 167–174.

LE BAIL, R. C. 1972 Use of fast Fourier Transforms for solving partial differential equations in Physics. *J. Comp. Phys.* **9**, 440–465.

LEONARDI, E. 1984 A numerical study of the effects of fluid properties on natural convection. Ph.D. thesis, University of New South Wales, Kensington, Australia.

LEONG, S. S. 1983 Natural convection in cylindrical containers. Ph.D. thesis, University of New South Wales, Kensington, Australia.

LEONG, S. S. & DE VAHL DAVIS, G. 1979 Natural convection in a horizontal cylinder. In *Numerical Methods in Thermal Problems* I (ed. R. W. Lewis & K. Morgan), pp. 287–296, Pineridge.

MALLINSON, G. D. & DE VAHL DAVIS, G. 1973 The method of the false transient for the solution of coupled elliptic equations. *J. Comp. Phys.* **12**, 435–461.

MALLINSON, G. D. & DE VAHL DAVIS, G. 1977 Three-dimensional natural convection in a box: a numerical study. *J. Fluid Mech.* **83**, 1–31.

MALLINSON, G. D., GRAHAM, A. D. & DE VAHL DAVIS, G. 1981 Three-dimensional flow in a closed thermosyphon. *J. Fluid Mech.* **109**, 259–275.

MARTINI, W. R. & CHURCHILL, S. W. 1960 Natural convection inside a horizontal cylinder. *AIChE J.* **6**, 251–257.

OSTRACH, S., LOKA, R. R. & KUMAR, A. 1980 Natural convection in low aspect ratio rectangular enclosures. In *Natural Convection in Enclosures*. HTD-8, pp. 1–10. ASME.

ROSENBERGER, F. 1980 Fluid dynamics in crystal growth from vapours. *Physico-Chemical Hydrodyn.* **1**, 3–26.

SCHIROKY, G. H. 1982 Free convection of gases in a horizontal cylinder with differentially heated end walls – a study by Laser Doppler Anemometry. Ph.D. thesis, University of Utah, Salt Lake City, Utah.

SCHIROKY, G. H. & ROSENBERGER, F. 1984 Free convection of gases in a horizontal cylinder with differentially heated end walls. *Intl J. Heat Mass Transfer* **27**, 587–598.

SHIH, T. S. 1981 Computer extended series: natural convection in a long horizontal pipe with different end temperatures. *Intl J. Heat Mass Transfer* **24**, 1295–1303.

SMUTEK, C., BONTOUX, P., ROUX, B., SCHIROKY, G. H., HURFORD, A., ROSENBERGER, F. & DE VAHL DAVIS, G. 1985 Three-dimensional convection in horizontal cylinders – numerical solutions and comparison with experimental and analytical results. *Num. Heat Transfer* **8**, 613–631.

SMUTEK, C., ROUX, B., BONTOUX, P. & DE VAHL DAVIS, G. 1983 3D-Finite Difference for Natural Convection in Cylinders. In *Notes on Numerical Fluid Mechanics* (ed. M. Pandolfi & R. Piva), vol. 7, pp. 338–345. Vieweg.

VAHL DAVIS, G. DE 1979 A note on a mesh for use with polar coordinates. *Num. Heat Transfer* **2**, 261–266.

WIRTZ, R. A. & TSENG, W. F. 1980 Natural convection across tilted, rectangular enclosures of small aspect ratio. *Natural Convection in Enclosures* HTD-8, pp. 47–54. ASME.